Absolute Cross Sections and Polarization for Electron-Impact Excitation of the K and H Resonance Lines of the Ca^+ Ion*

Paul O. Taylor† and Gordon H. Dunn

Joint Institute for Laboratory Astrophysics, University of Colorado and National Bureau of Standards, Boulder, Colorado 80302

(Received 12 July 1973)

Crossed beams of electrons and Ca^+ ions have been used to measure absolute cross sections for electron-impact excitation of the resonance K and H lines of Ca II at 3934 and 3968 Å, respectively. Polarization fractions of the light were also measured. The cross sections presented are absolute in the sense that all measurables including photon flux, have been compared to relevant standards. The cross section for excitation of the K line is observed to have a value of about $(18 \pm 2)\pi a_0^2$ at the 3.15-eV threshold, and to decrease to a magnitude of $(1.5 \pm 13)\pi a_0^2$ at 700-eV electron energy. Experimental uncertainties have been presented at the 98% confidence level, typically three standard deviations of random fluctuations combined in quadrature with the systematic uncertainties. The experimental results for both the K and H emissions are in agreement at 350 eV with the Coulomb distorted-wave calculation of Burgess and Sheorey but lie about 35% below the low-energy three-state close-coupling calculations of Burke and Moores. The ratio of the cross sections for the K and H emission is found to be 2.0 at all energies. Detailed study of the cross section at low energies demonstrates the expected finite value at threshold (within the accuracy allowed by the electron energy spread of 0.3 eV), and does not indicate the presence of a large (greater than 5%) contribution from cascade. Structure in the K cross section about 2 eV above threshold suggests interactions with autoionizing levels of Ca I, presumably belonging to the $5snl$ or $4dnl$ series. The polarization fraction at low energy is about 25% higher than the calculation of Saraph which is based on the Burke and Moores close-coupling calculation.

I. INTRODUCTION

Though electron-impact excitation of atoms[1] has been studied for more than 40 years, it is only quite recently with the advent of crossed-charged-beam techniques[2-4] that similar studies with ions have become possible. This is despite the importance of such cross sections in diagnostics and modeling of nonequilibrium plasmas. The need for understanding excitation of ions has resulted in considerable theoretical effort, which has led to progressively more sophisticated, and presumably more accurate, calculations of the cross sections. It became apparent that further theoretical progress awaited results from a few definitive experimental measurements to provide reference points against which theory might be judged. The goal of the present work has been to produce such a reference point, and the implied need for accuracy has played a major role in determining the care taken and the detail pursued in the experiment.

Previous cross-section measurements of electron-impact excitation of ions are limited to the crossed-beam studies on He^+, H_2^+, N_2^+, and Ba^+. The work[5] on He^+ dealt with the $1S$-$2S$ excitation which was observed by detecting photons resulting when an electric field quenched the metastable $2S$ state. The measurements were not absolute, but normalized to the Born approximation at several hundred eV. The work[6-8] on H_2^+ dealt mainly with the $1s\sigma_g - 2p\sigma_u$ excitation. Before the excited state can radiate, dissociation takes place, so detection was of the resultant proton. Results of these measurements are apparently quite accurately absolute.

The studies of N_2^+ and Ba^+ are the only previous ones in which cross sections for emission of dipole allowed radiation have been measured. The work by Lee and Carleton[9] on the emission of the first negative band of N_2^+ at 3914 Å was subject to a number of large systematic effects, and the results may be seriously in error. Bacon and Hooper[10] made relative measurements of the cross sections for exciting the resonance 4554 and 4934 Å transitions of Ba^+ at ten energies between 8 and 98 eV. Pace and Hooper[11] followed this up with absolute measurements at four electron energies (3, 4, 6 and 8 eV) for the 4554 Å transition. However, a low signal-to-noise ratio and the uncertainty of the optical calibration resulted in cross sections with uncertainties of about 30%, and use as the noted reference points is limited by this.

Choice of Ca^+ as the ion to be investigated here was prompted by the prominent role it plays in astrophysics. In particular, the H and K lines are important probes of solar and stellar chromospheres.[12] This active role has led to an unusual number and variety of theoretical calculations[13-18] on the excitation of this ion by electron impact, and thus it is an especially attractive

system to meet the aims of this work as mentioned above.

An energy-level diagram of Ca^+, which is isoelectronic with K, is shown in Fig. 1. The process to be studied is the bombardment by electrons of Ca II in the $4S_{1/2}$ state to give a resultant Ca II in the $4P_{3/2}$ or $4P_{1/2}$ state. These states have lifetimes of about 7 nsec, and the associated decay radiation at 3934 Å (K line) and 3968 Å (H line) is detected and measured. Thresholds for exciting the K and H lines are at 3.15 and 3.12 eV, respectively, and the cross sections are expected to have a finite value at threshold. Results of several calculations for excitation of the $4P$ multiplet are shown in Fig. 2. Nonunitarized calculations which are likely to greatly overestimate the cross section are left off the figure, as they would be well off the scale used.

Since cross sections for excitation of the different magnetic sublevels are, in general, not the same, the K line will be polarized.[19] This polarization is also measured in the experiment and compared to the calculations of Saraph.[20]

II. EXPERIMENTAL PROCEDURE

The experiment is to bombard Ca^+ target ions with variable energy electrons and measure a known portion of the photons resulting from excitation. This is accomplished by colliding well-collimated beams of the reactant particles at right angles and observing the light in a cone along the third orthogonal axis. The cross section is obtained from the equation

$$\sigma = \frac{1}{Y_\Omega}\,\frac{\mathfrak{R}}{I_i I_e}\,\frac{e^2 v_i v_e}{(v_i^2+v_e^2)^{1/2}}\,\frac{\mathfrak{F}}{D(z_0,\lambda)}\,. \tag{1}$$

Here σ is the emission cross section, $\mathfrak{R}$ is the recorded count rate of photons, e is the electronic charge, I_i and I_e are the total currents of ions and electrons, and v_i and v_e are the respective velocities. The anisotropy correction factor Y_Ω which includes allowance for the finite solid angle Ω of the detection system is given in terms of the angle θ between the direction of photon emission and the electron beam axis by

$$Y_\Omega = (1 - P\langle \cos^2\theta \rangle_\Omega)/(1 - \tfrac{1}{3}P), \tag{2}$$

where P is the polarization of photons emitted along the observation axis and $\langle \cos^2\theta \rangle_\Omega$ is the average value of $\cos^2\theta$ over the detection solid angle. The ion and electron beams are traveling in the x and y directions, respectively, and photons are observed in a cone along the z axis. The

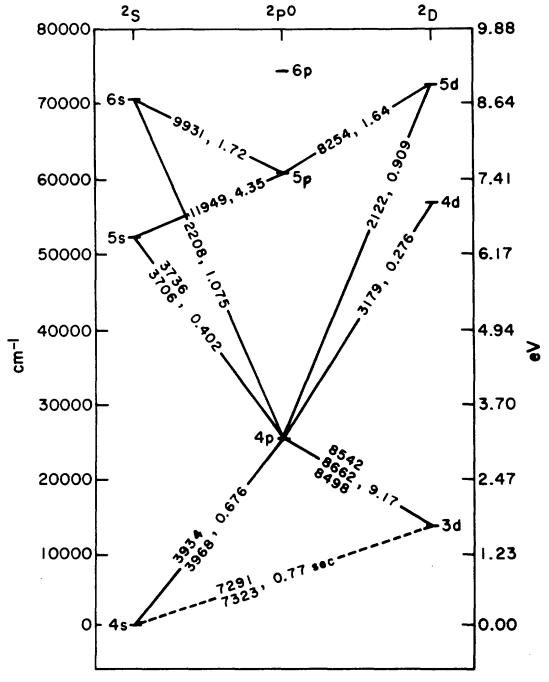

FIG. 1. Energy-level diagram of Ca II. Along lines indicating transitions are shown wavelengths in Å and lifetimes in 10^{-8} sec, except that the lifetime of the $3d \rightarrow 4s$ transition is 0.77 sec as indicated.

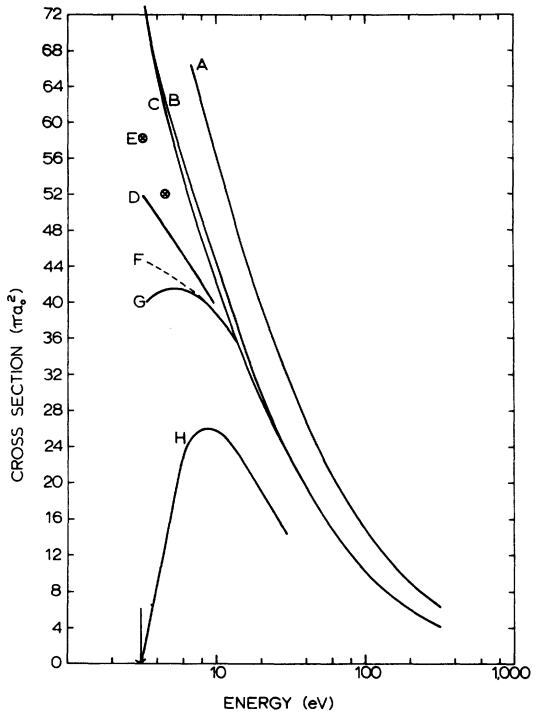

FIG. 2. Theoretical cross sections for electron-impact excitation of the $4s \rightarrow 4p$ transition in Ca II. A = Coulomb-Bethe (Ref. 18), B = Coulomb distorted-wave (Ref. 18), C = Coulomb-Born (Ref. 18), D = Coulomb-Born (Ref. 15), E = Coulomb-Born with allowance for coupling to third level (Ref. 14), F = close coupling ($4s$-$3d$-$4p$) without exchange (Ref. 16), G = close coupling ($4s$-$3d$-$4p$) with exchange (Ref. 16), H = classical binary encounter (Ref. 17).

form factor $\mathfrak{F}$ which accounts for the spatial overlap of the ion- and electron-beam density distributions $R(z)$ and $G(z)$ with the relative detection sensitivity profile $\eta(z, \lambda)$ can be written

$$\mathfrak{F} = \int R(z)dz \int G(z)dz \Big/ \int R(z)G(z)\eta(z, \lambda)dz , \tag{3}$$

where

$$\eta(z, \lambda) = D_R(z, \lambda) - I_1 + (e^{w_e/v_i\tau} - 1)I_2 , \tag{4}$$

and here

$$I_1 = \int_0^{w_e} e^{-x/v_i\tau} D_R(x, z, \lambda)\, dx \Big/ \int_0^{w_e} D_R(x, z_0, \lambda)\, dx , \tag{5}$$

and

$$I_2 = \int_{w_e}^{\infty} e^{-x/v_i\tau} D_R(x, z, \lambda)\, dx \Big/ \int_0^{w_e} D_R(x, z_0, \lambda)\, dx . \tag{6}$$

The quantity $D(z_0, \lambda)$ in Eq. (1) is the absolute average probability that a photon emitted in an arbitrary direction from the $z = z_0$ plane inside the collision volume will be recorded, and $D_R(z, \lambda)$ in Eq. (4) is the relative variation of that probability with height z such that $D_R(z_0, \lambda) = 1$. $D_R(x, z, \lambda)$ is the relative probability averaged over the width of the ion beam that a photon emitted from a line parallel to the electron beam will be detected, w_e is the mean width of the electron beam, and τ is the lifetime of the transition yielding photons of wavelength λ. The subtraction of I_1 accomodates for the fact that some particles do not radiate while within the limits of the electron beam. The term on I_2 is added to account for those which radiate beyond the limits of the electron beam but are still detected.

Equation (1) has the basic form widely encountered[2-4] in crossed-beam experiments, and the derivation is given in detail elsewhere.[21] The equation looks particularly like that used by Pace and Hooper,[11] as may be expected, except that the definitions of Y_Ω, $\mathfrak{F}$, and $D(z_0, \lambda)$ are different. This is because the work here allows for observing in a finite solid angle and for the finite lifetimes of the ion excited states, and also because the procedure in absolute calibration is different.

The polarization was obtained from the expression

$$P = [(C/I_i I_e)_\parallel - (C/I_i I_e)_\perp] / [(C/I_i I_e)_\parallel + (C/I_i I_e)_\perp] , \tag{7}$$

where $C_\parallel$ and $C_\perp$ are the counts in a set time obtained from photons of wavelength λ with a polaroid parallel and perpendicular, respectively, to the electron-beam axis. The beam currents are values integrated over the counting time.

Corrections to be applied to σ and P as calculated with Eqs. (1) and (7) will be discussed later.

It is a conceptually straightforward matter to proceed from Eq. (1), defining Eqs. (2)–(6), and from Eq. (7) to outline a measurement. One notes that the burden of the experiment is to accurately measure quantities appearing in these equations and to verify that there are no anomalous dependences on these quantities or other experimental parameters not appearing in the equations.

A schematic diagram of the experimental arrangement is shown in Fig. 3. Ca II formed by surface ionization is accelerated into a beam and mass analyzed. The 750-eV ion beam of about 0.1 μA is bombarded in a region of ambient pressure $\simeq 5\times10^{-10}$ Torr at right angles by a magnetically (~0.2 T) confined electron beam with energies ranging below 3 to 700 eV. Photons are collected with an F/2 lens system and made parallel after which those of the desired wavelength are selected with an interference filter. They are then refocused behind the cathode of a photomultiplier (PM) in a way that they illuminate about

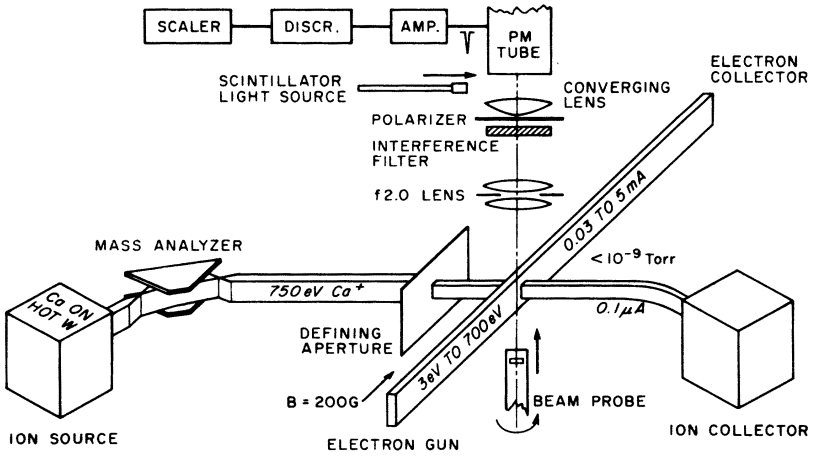

FIG. 3. Schematic of experimental apparatus.

80% of the 1-cm-diam photocathode and resultant PM pulses are counted. Both beams are probed at the crossing point to determine their spatial distributions, $R(z)$ and $G(z)$; and quantities entering into the determination of the relative detection sensitivity profile, $\eta(z, \lambda)$, are measured with movable monochromatic light sources. A polarizer can be inserted after the interference filter and rotated by 90° to allow measurement of P. Constancy of detection sensitivity of the PM can be monitored by inserting a radioactive scintillator source in the field of view of the PM. Ion and electron beams are square-wave-chopped at frequency f and $2f$, respectively, and the recording dual scalers are gated at frequency f, phase-shifted $\frac{1}{2}\pi$ and $\frac{3}{2}\pi$ with respect to the ion beam, thus allowing separation of signal and background events by the method of Bacon and Hooper.[10] Ion and electron currents are collected and measured with calibrated meters and the absolute optical sensitivity $D(z_0, \lambda)$ is measured using a uniform, nonpolarized, perfectly diffuse, and monochromatic light source of the same size as the beam crossover and placed at reference level z_0. This source was calibrated against a standard of radiance.

III. EXPERIMENT: DETAIL

Because of the absolute nature of the experiment and the goal of accuracy involved, considerable experimental detail is presented in this section. Additional details are discussed by Taylor.[21] The reader on the first time through, or the reader desiring less detail may wish to omit this section and go to Sec. IV.

A. Ion Beam

The primary concerns with the ion beam are beam purity, intensity, and beam geometry. Species purity is ensured by use of the 60° sector magnetic analyzer. Since there is a metastable state of the ion ($3\,^2D$), state purity will be determined by the type of ion source. To avoid appreciable $3D$ contamination of the beam, a surface ionization source was designed and used.

The source was built with the familiar Pierce geometry. The hot source was a 0.13-mm-thick W disk mounted in a large Mo electrode and with a 0.38-mm-thick by 6.35-mm-diam Ir disk spot welded in its center. The disk was heated by electron bombardment from behind with about 330 W of power to about 2000 °K or greater. Calcium atoms were directed onto the disk through channels in the extractor electrode from a Ca metal reservoir attached to the side of the electrode. Under these conditions the Saha-Langmuir equation predicts a few tenths of a percent ionization efficiency (depending on the exact value of the work function) and a maximum metastable to ground-state ion ratio of 1×10^{-3}. Total currents of a few microamperes were obtained from the source, but the well-collimated beam in the collision region was only 0.1 μA. The source charge lasted for about 100 h of operation, and over this period the beam was stable and reproducible. Mass scans of the beam routinely indicated low levels of Na_{23} and K_{39} (<1%), and the normal abundance ratios of Ca_{40}, Ca_{42}, Ca_{44}, and Ca_{48}.

After extraction and focusing through a 2.4-mm hole, the beam traverses optics very similar to that described earlier,[6] except that after passing through the collision region it is bent by a 127° cylindrical analyzer into a 5-cm-deep collector cup preceded by slits for retarding secondary electrons. A total current of less than 0.35% of the ion-beam current was recorded to all surfaces between the collision box and the ion collector. Ion currents are typically measured by integrating the voltage developed across a precision resistor. This integration is carried out with operational amplifiers throughout the entire photon counting period and the system is calibrated to better than 0.5% using standard techniques.

The ion beam is about 2.5-mm wide by 7.6-mm high (base of distribution measurements) with about 0.3° divergence at the interaction region, and it can be readily positioned within the electron beam. Photon background counts produced by the ion beam's hitting background gas or surfaces is less than 1 sec^{-1}, making modulation of the electrons of marginal utility in this experiment. There was a 10.4-μsec time delay between ion-beam switching and electron (and scaler) switching to allow for the measured 10.4-μsec transit time of ions from their switching plates to the collision region.

The ion velocity v_i appearing in Eq. (1) is simply that characteristic of the potential difference between the collision region and the hot surface where ions are formed.

B. Electron Beam

Because of the low target density ($\sim 5\times10^5/\text{cm}^3$) and a detection efficiency less than 10^{-3} counts per photon produced, it is highly desirable to have an electron beam of substantive intensity in order to get signal levels of workable magnitude. It is also desirable that the gun work at energies below threshold (3.1 eV) and have an energy spread small compared to this energy. In addition, the cathode ought to be optically removed from the light detection system, and the collision volume must be large enough to insert a beam probe. The

beam must be well defined and not change its distribution rapidly with energy, and of course there should be a minimum of secondary electrons in the beam and reliable total electron collection.

These specifications led to the adoption of a magnetically confined ribbon beam of electrons 2-mm wide by 10-mm high. The gun used to produce this beam is shown in Fig. 4 and also discussed elsewhere.[21,22] The gold-plated superstructure is made up of four 1.27-cm-diam-Alnico rod magnets (2) centered on the corners of a 5.08-cm square and terminated by 8.89-cm-diam Armco iron pole caps (1). Support plates (3) for the e-gun mount from the magnets, and the gun electrodes mount from the support plates. The variation of the axial magnetic field is shown by the dashed curve with ordinate scale on the left. The beam size is limited by the 2 mm×10 mm slit in GC located only 0.38 mm from the cathode. Voltages vary linearly with distance from the cathode. The collector includes an Inconel "honeycomb" mounted at an angle and made of cells open at both ends about 1.5-mm diam, with 0.025-mm walls, and about 3 mm deep. Most surfaces of the gun are coated with gold black.[23] The collision box (4) is 3.81 cm square by 2.54 cm deep and contains slots for ion- and electron-beam passage, a 1-cm-diam hole in the bottom for the beam probe, and a 1.5-cm hole in the top for light to exist. Typical currents to various electrodes under normal operating conditions are shown in Table I. Beam current is taken as that to the collector plus that to electrodes $G5$ and $G6$ and measured in the collision experiment in the manner described above for ions. The beam is very stable and is readily modulated with a square wave applied to $G1$.

Use of such a beam has some inherent problems: (i) space-charge energy shift and broadening in such beams is generally high and (ii) the spiraling of electron trajectories about the magnetic field lines means the electrons are traveling at some angle γ with respect to the beam axis. This in turn implies corrections to the beam-path length, the polarization, and the interaction energy. Thus, these effects were examined in some detail.

It was determined that the true average energy in the beam could be accurately represented by

$$eV_e = e[V_c - \phi(V_e) - (S/V_e^{1/2})I_e], \tag{8}$$

where V_c is the cathode potential in volts, $\phi(V_e)$ is basically a contact potential difference, I_e is electron current in milliamperes, and S is a constant depending on geometry having the value $0.102(\pm 7\%)\ V^{3/2}/\mu A$. This relationship is consistent with the theory of Haeff[24] for long, tall, thin beams and with what one calculates[21] for cylindrical beams except that the geometric constant S is different. This equation was verified and the constants S and ϕ determined by observing threshold functions for optical excitation for a broad range of I_e at 3 eV (Ca II), 23.0 and 24.3 eV (He), and 75.6 eV (He^+). These measurements gave S

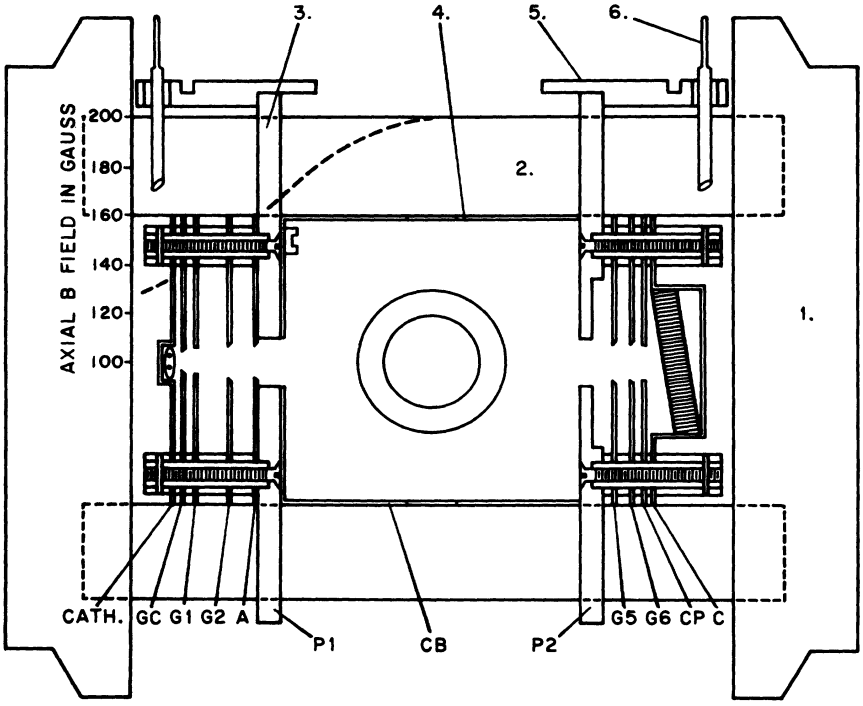

FIG. 4. Plan view of electron-gun structure. The top plate (5) and electrical contacts (6) are shown rotated from their true orientation relative to the other parts by 90°. Electrodes are labeled as referred to in the text. The axial magnetic field strength as a function of longitudinal position is shown superimposed on the diagram.

TABLE I. Currents to the collector and the electrodes $G5$ and $G6$, CB, and $G2$ for normal gun conditions.

V_{GC}	V_{cath}	Collector μA	$G5+G6$ μA	%	CB μA	%	$G2$ μA	%
96% V_{cath}	20	100	0.05	0.05	0.02	0.02		
	50	340	0.6	0.18	0.32	0.09		
	100	840	4	0.48	3.2	0.38	2	0.24
	150	1470	16	1.1	10.5	0.71	6	0.41
	200	2180	33	1.5	23	1.1	13	0.60
	250	3230	40	1.2	38	1.2	26	0.80

as above, and $\phi = 2.0$ V, with only a small energy dependence in ϕ.

With the same set of threshold measurements, and comparing with other parts of the same theories, the energy spread was shown to be

$$\Delta V_e = \Delta V_{th} + S' I_e / V_e^{1/2}, \tag{9}$$

where here ΔV_{th} is the width exclusive of space charge (primarily thermal) with a value of 0.22 V, and S' is another constant with value 0.021 (±10%) $V^{3/2}/\mu A$.

Equations (8) and (9) were used in this experiment at all energies and currents to arrive at the true values of energy and energy spread.

In magnetically confined beams, electron velocity transverse to the beam (magnetic field) axis is manifest as spiraling about the field lines with diameter $D = 67.4\ V_\perp^{1/2}/B$, at the cyclotron frequency $\omega_c = 1.76\times10^7 B$, and a pitch $P = 212 V_\parallel^{1/2}/B$. Here D and P are in mm, the magnetic field in gauss, and $V_\perp$ and $V_\parallel$, the kinetic energies associated with perpendicular and parallel velocities, respectively, are in eV. The pitch angle is given by $\sin\gamma = (V_\perp/V_e)^{1/2}$ where $V_e = V_\perp + V_\parallel$.

In such trajectories, the electrons travel longer paths in covering the axial distances L_0, the path being increased by the factor $\sec\gamma$. For $V_\perp/V_e \ll 1$ the change in path length ΔL is then given[25] by

$$\frac{\Delta L}{L_0} = \frac{\gamma^2}{2} = \frac{V_\perp}{2V_e} = 1.1\times10^{-4}\frac{D^2B^2}{V_e}. \tag{10}$$

Similarly, the polarization of light excited by electron impact, observed orthogonal to the beam axis, is[21]

$$P_\gamma = P(1 - \tfrac{3}{2}\gamma^2)/(1 - \tfrac{1}{2}P\gamma^2), \tag{11}$$

where the small-angle approximation has again been used. Here P_γ is the polarization observed due to impact of electrons traveling at angle γ with respect to the axis and P is the value when γ is 0.

The center-of-mass energy also depends on γ, and for the conditions of this experiment leads to a small-energy broadening according to the expression for the center-of-mass energy (in eV for 750 eV CaII):

$$V_{c.m.} = V_e + 0.01 \pm 0.2 V_e^{1/2} |\sin\gamma|. \tag{12}$$

It is thus clear that to make proper corrections to the data through Eqs. (10) and (11), a knowledge of γ, or equivalently D or $V_\perp$ is needed. Prior work[25-28] on this problem is not adequate to allow evaluation of γ, making it necessary to further evaluate and model sources of spiraling and to develop a technique to measure D.

As discussed in depth elsewhere[21,22] the main source of spiraling at low energies is the thermal transverse velocities of electrons at the cathode. For the conditions of this experiment one predicts from this source $\langle \frac{1}{2}\gamma^2 \rangle_T = 0.7\ kT/V_e$. Transverse velocities induced at the anode lens lead to $\langle \frac{1}{2}\gamma^2 \rangle_A = 0.0006$, and transverse electric fields at the cathode give $\langle \frac{1}{2}\gamma^2 \rangle_C = 0.0003 + 0.007 V_B/V_e$. Angular brackets indicate averages over the distribution of spiraling diameters, T is the cathode temperature, V_B is a bias on G_c (usually 0–1.5 V), and V_e is the electron energy. At high energies these are the dominant sources of spiraling. Space charge in the beam plays a negligible role in spiraling and magnetic-field gradients have been accounted for in the relations given.

Measurements of the spiral diameter were made in the following way.[22] If a beam of electrons with spiral diameters D is intercepted by a channel of height H and thickness T, then if the maximum diameter is less than H, the total current transmitted is $I(H) = J[H - \langle D\rangle g(T/P)]$. Here J is current per unit height, $\langle D\rangle$ is the average diameter, and $g(T/P)$ is a function of the ratio of channel thickness to spiral pitch, being a calculable constant for a given electron energy. Measurements of transmitted current for different H, when plotted, yield a curve which for large enough H goes to a straight line whose intercept with the H axis is just $\langle D\rangle g(T/P)$. With $\langle D\rangle$ determined and some knowledge of the distribution of diameters one can calculate $\langle \Delta L/L_0 \rangle$ from Eq. (10).

Figure 5 shows percentage path-length correction as a function of energy. The theoretical curve labeled as quadrature represents the result of summing predicted path-length corrections from various sources (and is thus equivalent to combining the average diameters in quadrature). The curve labeled "direct sum" is the average path-length correction obtained from the direct sum of all the predicted diameters, and should be an overestimate of the actual path-length correction. Consideration of the inadequacies in both the experimental and theoretical treatment of spiraling led to the adoption of a curve lying between the extremes of theory and experiment to be used for data correction. An uncertainty is allowed which more than covers the extremes.

Determination of the total electron current in the beam involves an assessment of the role of secondary and backscattered primary electrons. Electrons striking the beam-defining slit GC have only 4% of the final beam energy, and are thus inefficient producers of secondary electrons. Any secondaries that are produced here will have an energy only 4% below the nominal beam energy, and their efficiency in exciting ions will be only slightly different from the main beam. This effect is thus ignored. Measurements of the beam profiles at the center of the interaction region show that the beam is well collimated by the magnetic field; and is, as expected, slightly smaller at the interaction region than at the defining slit because of the converging magnetic field. There is thus little reason to believe that currents to other electrodes in the acceleration stage of the gun are due to primary beam. The beam, upon arriving at the collector end, can be collected, it can produce secondary electrons, or it can be backscattered. The honeycomb collector was chosen to "trap" those secondaries and backscattered primaries originating within the depths of the honeycomb cells. Those originating on the front structure of the honeycomb (5–10% of the area) could, however, exit the collector and retraverse the collision region still confined by the magnetic field. If a positive bias is put on the collector, low-energy secondaries produced at the collector will be trapped. A plot of current to various electrodes as a function of collector bias (at energies high enough to produce secondaries efficiently, e.g., 200 eV) shows a collector current about 10% low at zero bias and rising rapidly to 99% of the saturated value by about 25-V bias. The current to $G5$ and $G6$ drops very rapidly at first (0 – 25 V), and then continues to change slowly with bias out to 250 V. Currents to other electrodes generally change slowly with the bias.

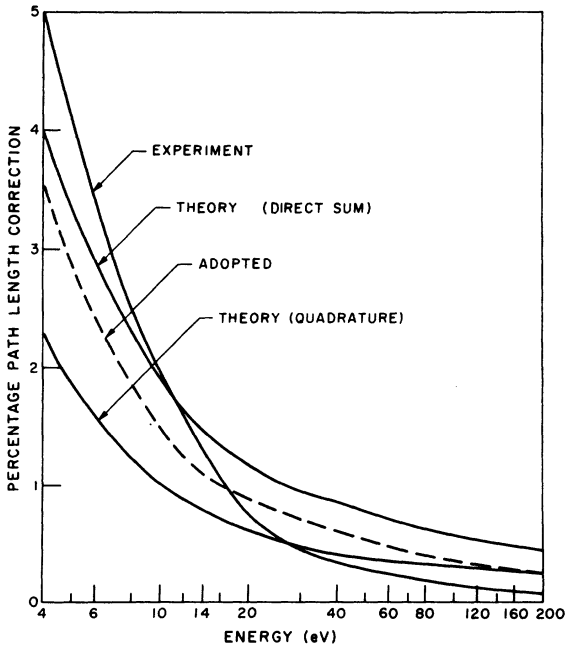

FIG. 5. Path-length correction (in percent) as a function of electron energy. The correction derived from experimentally measured spiraling diameters is compared with the corrections predicted from theory (combined in two different ways). The correction adopted for adjusting the cross sections is a compromise between theory and experiment.

Assuming the secondary electron yield[29] at the collector to be 0.5–1, the evidence is that only 5–10% of the low-energy secondaries escape the collector at zero bias—a figure consistent with the front area of the honeycomb. Most of these secondaries are intercepted by $G5$ and $G6$. A fixed bias of +130 V is put on the collector, ensuring that low-energy secondaries from the collector do not escape.

The fraction of the beam backscattered from the collector will typically lie[29] between 0.1 and 0.3. The honeycomb trapping may allow 5–10% of these to escape, meaning 0.5–3% of the beam leaves the collector. About half of this will be intercepted by $G5$ and $G6$ because of the large spiraling diameters induced by backscattering and transverse fields at the collector. The 0.25–1.5% of the primary beam that escapes the biased collector and electrodes $G5$ and $G6$ may retraverse the collision region, necessitating a correction to the beam current of between 0.5 and 3%. If not collected on another electrode such as $G2$ or the anode, these electrons may traverse the beam a third time, but then are likely to be collected and measured with the normal current so that the correction stays the same. Those electrons of this group which do hit another electrode may generate secondaries. Such secondaries may effectively become part of the beam and, since the cross section for these lower-energy particles is greater, they can have an amplified effect on the excitation. For example, if 1% of the beam hit the anode at 250 eV, and the secondary-electron yield on the gold-blacked surface is 0.5, then 0.5% of the electrons could have a low energy where the cross section is about 5 times as high. The cross section could then be overestimated by 2.5%.

Such considerations have led to the following procedure. The current is measured as that to $G5$, $G6$, and the collector and an uncertainty is allowed large enough to include all or most of the current to CB and $G2$. For energies above 50 eV an additional one-sided uncertainty shown in Table II is allowed for the effects of the electrons not

TABLE II. Maximum additional uncertainty which may arise from the presence of low-energy secondaries in the electron beam.

Cathode potential V_C (V)	Uncertainty %
100	+0, −2.7
120	+0, −3.0
150	+0, −3.5
200	+0, −4.0
250	+0, −5.0
350	+0, −8.0
700	+0, −20.0

trapped at the collector. Work done after the measurements reported here indicates that this latter one-sided uncertainty is probably too large. Thus, it was recognized that space charge in the beam causes a vertical shear, and that by the time the beam reaches $G5$ and $G6$ the beam may not pass through the slit at the upper and lower ends. Elongating these slits by about 2 mm reduced the currents to $G5$ and $G6$ by about a factor of 3 or 4 and at the same time reduced the current to CB by a factor of 6 and the current to $G2$ was reduced by more than a factor of 10. Thus, it is likely that most of the current to CB and $G2$ came from secondaries and backscattered primaries from $G5$ and $G6$ at the extreme ends where they would not encounter the ion beam on their recurrent passages through the collision region.

C. Beam Profiles

The beam profiles $R(z)$ and $G(z)$ appearing in Eq. (3) were measured by observing the currents transmitted through a 0.15-mm slit as the slit was scanned through the relevant range of z. This is basically the method which has become traditional, except that the beams were scanned at the position of intersection rather than some distance away, as by the usual L-shaped probe.[6] This was accomplished by using a single slit which could be rotated to probe either beam, and was necessitated by uncertainties of magnetic field gradients, beam shear caused by space charge, etc. Profiles were measured for all data points except those obtained in closely spaced energy scans near threshold. Here, profiles were measured at selected energies throughout the 14-eV energy range, and an interpolation was made of the form factor which varied monotonically by only 6% through this range.

D. Photon Detection and Data Acquisition

The photon detection system is indicated schematically in Fig. 3. Photons are collected through a pair of 52-mm-diam lenses with focal lengths of 106 mm and with a 27-mm aperture stop between them at a distance of 53.6 mm from the center of the collision volume. Ray tracing shows all observable photons to be collimated within about 3° of the optic axis as they pass through the vacuum window and then through an interference filter, the next elements in their path. The K-line filter has a transmission centered at 3931 Å with a full width at half-maximum of 16 Å and a nominal transmission at 3934 Å of 22%. The H-line filter is flat topped and centered near 3968 Å with a 30 Å width and transmission at the H line of about 23%. Since there is typically a shift in filter characteristics of about 0.1 Å per degree centigrade, an effort was made to use the filters only after thermal equilibrium to the same temperature had been reached. The fact that some rays traverse the filter at up to 3° from the normal is accounted for by the calibration technique described later. The polarizer, inserted next in the path only during polarization measurements, has a measured polarizance $K = 0.98 \pm 0.005$. This quantity[30] relates the polarization of the light emerging to the incident polarization according to $P_{\text{obs}} = KP_{\text{inc}}$, and is needed to correct the observed polarization for nonzero transmittance of light polarized perpendicular to the axis.

The light is next converged by a lens onto the 1-cm-diam photocathode of the photomultiplier tube. The tube is in a commercial housing and cooled to about −25°C by flowing cold N_2 past it, and at this temperature the dark count is about 2 sec^{-1}. Pulses from the PM are amplified (×100) and fed into a disciminator from which the 0.5-μsec uniform pulses enter one of two gated scalers. Routine pulse-height analysis indicated that 96% of the pulses were counted by the scalers. Measured dead time of the system is $\tau_D = 0.56 \pm 0.07$ μsec, and necessitates obtaining the true count rate C from the measured rate C_M according to $C = C_M/(1 - \tau_D C_M)$. This amounts to about 1% correction to some of the count rates (2×10^4 sec^{-1}) encountered during calibration.

Two different PM tubes were used, and were investigated thoroughly as to temperature dependence of sensitivity and spectral response and to uniformity of response over the photocathode. Operating conditions were chosen to obviate errors from these sources. Relative sensitivity of the multiplier could be monitored by a stable light source consisting of a plastic scintillator excited by β^- emission from Tl^{204} ($T_{1/2} = 3.82$ yr). Natural decay was taken into account in evaluating the PM sensitivity, and a temperature dependence of −0.8% per 10°C was accounted for in setting allowable temperature variations. Multiplier sensitivity was very stable from day to day, variations being typically less than 1%.

Data are accumulated for a preset integration period accurately controlled by a 100 kHz "clock," after which integrated ion and electron currents, electron energy, and counts in both scalers are recorded. The phase of the electron switching is then changed 180°, and another integration made at the same energy. This can continue for an arbitrarily long time, or other experimental parameters can be varied, e.g., electron current, chopping frequency, pressure, electron energy, etc. The electron energy can be automatically advanced, so that scans of cross section as a function of electron energy can be effectively taken automatically over long periods (e.g., overnight). At 90-eV corrected electron energy, with average electron and ion currents 830 and 0.042 μA, respectively, signal plus background counts total about 5000 and background counts about 400 for a 100-sec integration period. This is somewhat representative; except that, of course, signal and background are both increasing functions of electron energy when allowance is made for increasing current with energy.

E. Radiometry

The remaining quantities in Eq. (1) needed for determination of the cross section are $D(z_0, \lambda)$ and $\eta(z, \lambda)$ [Eqs. (4)–(6)]. Techniques developed for determination of these radiometric terms are described[21] elsewhere in more detail than is possible here, including a discussion of fundamental differences with the method of Pace and Hooper.[11]

As noted in Sec. II, a uniform, nonpolarized, isotropic, and "monochromatic" light source of the same area as a cross section through the intersecting beams was developed and used for determination of $D(z_0, \lambda)$. This source was realized with a 150-W quartz-iodide lamp illuminating the entrance of a 35-cm grating monochromator set for a 2.5 Å bandpass, a 2-mm-diam quartz light pipe at the monochromator exit slit and a 1-cm-diam integrating sphere at the terminus of the light pipe. The uniformity and isotropy of the sources were investigated in detail, and only very small corrections had to be applied for imperfections. The intensity level was low enough that it could be placed directly in the collision volume without going into a nonlinear range of the detection system ($\sim 2\times 10^4$ Hz) yet great enough that it could be compared directly with a low-temperature blackbody.

The procedure was to calibrate this transfer standard against a vacuum tungsten strip lamp whose spectral radiance had previously been matched against a Cu point (1357.8°K) blackbody.[31] All intercomparisons (blackbody-strip lamp-transfer source) were made with a spectroradiometer consisting of a grating monochromator with lens preoptics, an interference filter to cut out light in the far wings of the monochromator slit function, a cooled photomultiplier with counting electronics, and stable reference light sources to monitor stability. The response to the calibrated transfer source placed at a well-defined position in the collision volume was then recorded.

One can show that the relationship between the needed sensitivity $D(z_0, \lambda)$ and quantities involved in the intercomparison is

$$D(z_0, \lambda_M) = \frac{1}{4\pi A_\Omega} \frac{C_S(\lambda_M)}{L_S(\lambda_M)} \frac{C_F(z_0, \lambda_M)}{C_C(\lambda_M)} \frac{I_C}{I_S I_F}. \tag{13}$$

Here A_Ω is the average projected area $\langle \sin\theta \rangle_\Omega A$ of the transfer source as seen by the detector in the collision apparatus, $C_F(z_0, \lambda_M)$ is the count rate observed with the transfer source in the collision apparatus at height z_0 and x-y coordinates the same as the beam intersection, $C_C(\lambda_M)$ is the count rate when the spectroradiometer views the transfer source, $C_S(\lambda_M)$ is the count rate when the spectroradiometer views the strip lamp of radiance $L_S(\lambda_M)$, and the quantities I_F, I_S, and I_C are given by

$$I_F(\lambda_M) = \int_0^\infty W_R(\lambda)\, T_R(\lambda)\, t(\lambda, \lambda_M) D_R(z, \lambda) d\lambda, \tag{14}$$

$$I_S(\lambda_M) = \int_0^\infty L_{SR}(\lambda) R_R(\lambda)\, s(\lambda, \lambda_M) d\lambda, \tag{15}$$

$$I_C(\lambda_M) = \int_0^\infty W_R(\lambda)\, T_R(\lambda) R_R(\lambda)\, t(\lambda, \lambda_M)\, s(\lambda, \lambda_M) d\lambda. \tag{16}$$

In these last equations the subscript R denotes that the function gives the relative variation with wavelength, and normalization is such that the functions have value 1 at $\lambda = \lambda_M$. The functions $t(\lambda, \lambda_M)$ and $s(\lambda, \lambda_M)$ are the normalized slit functions of the transfer source monochromator and spectroradiometer monochromator, respectively, $W(\lambda)$ is the spectral radiance of the quartz-iodide lamp for the transfer source, $T(\lambda)$ is the transmission of the monochromator-light pipe-integrating sphere combination, and $R(\lambda)$ is the effective spectral response of the spectroradiometer.

In practice the integrals I_F, I_S, and I_C were evaluated numerically using measured functions. It is useful, however, to examine the approximate magnitudes and behavior of these terms. If it is noted that $t(\lambda, \lambda_M)$ and $s(\lambda, \lambda_M)$ are narrow compared to the range for rapid variation of the other functions, then these other functions can be replaced by straight lines. If further, the slit functions are replaced by "best fit" triangles, then the

integrals can be evaluated numerically. When this is done, one gets to first order (second-order terms are less than 0.01%) $I_S = \Delta\lambda_R$, $I_F = \Delta\lambda$, and $I_C = (1 - \Delta\lambda/3\Delta\lambda_R)\Delta\lambda$, where $\Delta\lambda_R$ is the bandwidth of the spectroradiometer and $\Delta\lambda$ is the bandwidth of the source monochromator. The factor $I_C/I_S I_F$ in Eq. (13) was 3% smaller when evaluated in this approximate way than when numerical integrations were made of the measured function. Most of this difference comes from the approximation of the slit functions by triangles in the integral I_C.

Calibration transfers [i.e., determination of C_F/C_C in Eq. (13)] were carried out about 10 times at each λ, and exhibited a standard deviation about the mean of 1.9%. Uncertainties from individual sources such as counting statistics, light-pipe flexing, light-pipe removal and replacement, use of scintillator to normalize sensitivity, etc. were carefully evaluated; and when combined in quadrature these lead to an over-all uncertainty in a single calibration transfer of 6% (98% CL). It is significant that the observed total scatter and this number predicted from individual sources are in agreement, and that the scatter in all the observations appears to fit a normal distribution. Systematic uncertainties in the evaluation of C_F/C_C were carefully measured in separate experiments, or determined from analysis of the data, and at the 98% confidence level are: setting of wavelength in $C_C(\lambda_M)$ [0.5%], setting of wavelength in $C_F(z_0, \lambda_M)$ [2.3%], rotation of sphere head (necessary in transferring from spectroradiometer situation to crossed-beam apparatus) [0.6%], nonuniformity of transfer source emitting area [1.0%], size of source and scattered-light effect (in comparison of transfer source-strip lamp-blackbody) [1.0%].

Final evaluation of the data gives $D(z_0, 3934\ \text{Å}) = 3.4\times10^{-4}$ (±5.6%) counts/photon and $D(z_0, 3968\ \text{Å}) = 4.0\times10^{-4}$ (±5%) counts/photon. The uncertainties are again at the 98% confidence level (about three standard deviations). If one predicts the quantity $D(z_0, \lambda)$ on the basis of geometry, transmission, manufacturer's quantum efficiencies, etc., the results are $D(z_0, 3934\ \text{Å}) = 3.1\times10^{-4}(^{+30}_{-50}\%)$ counts/photon and $D(z_0, 3968\ \text{Å}) = 3.2\times10^{-4}$ (±30%) counts/photon. One sees that within their large uncertainty the predicted values are reasonable.

The relative optical calibration consists of determining the response of the optical detection system to photons of the wavelength of interest, as a function of point of origin in the emission volume. The cross-section equations [(1)–(6)] are expressed in such a form that two spatial sensitivity functions are required. The main function $D_R(z, \lambda)$, is determined by stepping along the z (optic) axis in the collision volume a diffuse source of photons of wavelength λ, whose area approximates the cross-sectional area of the collision volume. The function $D_R(x, z, \lambda)$, which enters into minor terms allowing for the finite time between excitation and photon emission, is measured by stepping a line source in both the x (ion beam) and z directions throughout the emission volume. The scanning source is similar to that used for absolute calibration, except that the terminus is changed.

Results for $D_R(z, \lambda)$ show a nearly linear function for 6 mm on either side of z_0 with a slope for the K filter of 3.4% per mm. If the integral terms in Eq. (4) are regarded as corrections to $D_R(z, \lambda)$, then the measured correction varies over the height of the ion beam from about 0.3% at the bottom to 1.7% at the top.

F. Consistency Checks

It is important to demonstrate that the functional relationships of Eq. (1) are obeyed, and that there are not spurious dependences on other experimental parameters—i.e., it is important to verify that the "theory of the experiment" is valid for the measurement.

The background pressure in the collision tank was varied over a range of vacuum gauge readings which ran from 4.3×10^{-10} Torr to 1×10^{-8} Torr, probably corresponding to a pressure change of 1×10^{-10} Torr to 1×10^{-8} Torr. The background associated with electrons at 100 eV varied between 6 and 660 sec^{-1}, and the signal-to-background ratio varied from about 10–0.07 over this range. Measurements were made at five pressures, and the cross section was constant to within 1%—i.e., within the statistical uncertainty of these measurements.

The cross section was also shown to be independent (to the 1% level) of modulation frequency over the range 100 Hz to 6 kHz. Cross sections measured with a continuous ion beam were the same, within counting statistics, as those obtained with both beams pulsed.

Moving the ion-beam vertical position provided a means for changing the form factor $\mathcal{F}$, since both the electron-beam vertical current distribution and the relative vertical spatial sensitivity, which occur in $\mathcal{F}$ [Eq. (3)], change with position. The signal was measured for 5 ion-beam "positions" ranging from 1.12 mm below the "normal" position to 2.5 mm above. The form factor changed from 1.123 cm at the lowest position to 0.860 cm at the highest. The relative cross section was independent of ion-beam position within the uncertainty of ±1% (SD) resulting from counting statistics.

In order to determine the sensitivity of the

cross-section measurements on the horizontal position of the ion beam, the beam was deflected to several horizontal positions within ±1 mm of the "normal position." The form factor $\mathfrak{F}$ and the signal were measured at each position. $\mathfrak{F}$ remained constant within about 0.5% until the ion beam was deflected so far in one direction that part was lost to the entrance slit to the collision box (and even then it was only 1.2% lower than at the normal position). The relative cross section showed little significant change, within the statistical uncertainty of ±1% (SD), until the beam was deflected beyond 0.5 mm from the normal position. At the extreme positions the relative cross section was down about 3%. These results are consistent with relative spatial optical sensitivity measurements similar to those referred to in Sec. III E. Since there was no precise way of setting the ion-beam horizontal position with respect to the position set in the absolute calibration, an uncertainty of 2% (98% CL) was allowed for possible changes in sensitivity with horizontal ion-beam position.

Electron current was varied over a significant range, and when corrections were made for the change in energy due to space charge according to Eq. (8), accurately linear behavior of signal

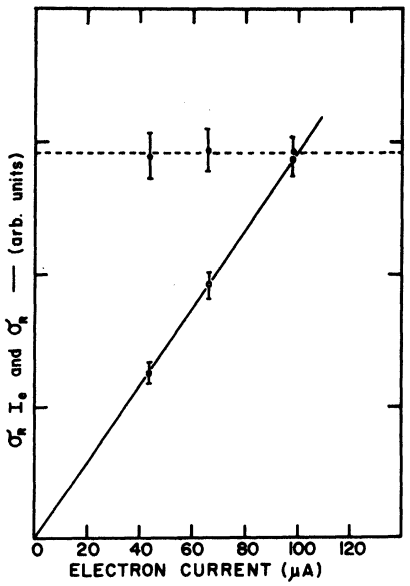

FIG. 6. Dependence of relative cross section on electron-beam current at an electron energy of 13.3 eV. Points shown are those obtained after correction for space-charge depression of the potential in the electron beam. Flags represent three standard deviations of the statistical fluctuations combined in quadrature with the simple sum of the systematic uncertainties which enter into the relative cross section. The cross section times current is also shown along the solid sloped line.

versus current was obtained. Many of the final data points were obtained as the slopes of such lines. An example of such a plot at 13.3 eV is shown in Fig. 6. Similarly the cross section was found to be independent of ion current.

The ion energy was varied between 535 and 984 eV, corresponding to a change in v_i in Eq. (1) of 36%, and the cross section was found to be constant to ±2%, within counting statistics and form-factor uncertainty for this measurement. It was shown with repeated scans of electron energy to as low as 0.5 eV that the signal below threshold for $4P$ excitation is zero. This confirms that $3D$-state content of the beam is negligible, and that unknown spurious effects due to electrons interacting with ions are not significant.

Data showing the dependences discussed in this section are given graphically elsewhere.[21]

G. Corrections

There are several corrections which must be applied to the data beyond those associated with calibrations. Corrections for counting dead time and background are obvious, and were made in early stages of data reduction. Electron-energy corrections for space-charge depression and contact potential have already been discussed in Sec. III B.

The polarization given from Eq. (7) must be corrected for the polarizance of the polaroid as discussed in Sec. III D, giving for our case $P' = 1.013P_0$. Next, it is necessary to correct for leakage of the unwanted line through a given filter. For the K line this gives $P''_K = 1.0035P'_K$. The polarization is "smeared out" by virtue of viewing in a finite solid angle, and for the $f/2$ optics of this measurement we get $P''' = P''/[1 - 0.015(1 - P'')]$. Finally, a correction must be made for smearing due to the spiraling trajectories of the electrons according to Eq. (11), giving $P = P'''/[1 - \Delta L/L_0 \times (3 - P''')]$.

An analogous set of corrections must be applied to the cross section. To account for spiraling the anisotropy factor becomes $Y_\Omega = Y'_\Omega[1 - P(\Delta L/L_0)]$, where Y'_Ω is as given in Eq. (2). The cross section must be divided by $(1 + \Delta L/L_0)$ to account for path-length increase due to spiraling. To correct for leakage of the unwanted line of the multiplet, e.g., H line through the K-line filter, the respective cross sections must be divided by a factor T. We have, for the respective cases:

$$T_K = 1 + \frac{D_K(z_0, \lambda_H)/F_K(\lambda_H)}{2Y_{\Omega K} D_K(z_0, \lambda_K)/F_K(\lambda_K)} = 1 + \frac{0.0035}{Y_{\Omega K}}$$

and

TABLE III. Significant sources of uncertainty in the relative cross-section measurements. Random uncertainty is at the 98% confidence level. Systematic uncertainties have been taken sufficiently large to be considered at the 98% CL also. DS ≡ direct sum; Quad ≡ combined by quadrature where warranted (see Sec. IV).

Source of uncertainty	Percentage uncertainty 4 eV DS	4 eV Quad	98 eV DS	98 eV Quad
Random uncertainty in $\sigma_R(E)$	4.0	4.0	2.5	2.5
Systematic uncertainty in $\sigma_R(E)$				
Anisotropy correction factor	2.0		0.4	
Form factor	2.0		2.0	
Path-length correction	2.0	6.2	0.2	4.1
Uncollected electron current	0.2		1.5	
Additional uncertainties in $\sigma(E)$				
Scintillator use	1.0		1.0	
Horizontal ion-beam position	2.0		2.0	
Temp. of KN filter	2.3		2.3	
Electron-current instrumentation	1.0	3.6	1.0	3.6
Ion-current instrumentation	1.0		1.0	
Ion velocity	0.5		0.5	
Filter transmission correction	0.3		0.3	
Total uncertainty in $\sigma(E)$ excluding absolute optical calibration	18.3	8.2	14.7	6.0

$$T_H = 1 + \frac{2Y_{\Omega K} D_H(z_0, \lambda_K)/F_H(\lambda_K)}{D_H(z_0, \lambda_H)/F_H(\lambda_H)} = 1 + \frac{0.034}{Y_{\Omega K}} .$$

The factor $Y_{\Omega K}$ ranges from 1.076 at 3.3 eV to 0.941 at 690 eV.

IV. UNCERTAINTIES

Evaluation and statement of uncertainties has played an important role throughout the measurement. An attempt is made in this section to define terms and procedures used and to summarize dominant uncertainties.

Commonly used methods and definitions[32] are applied to the handling of statistical imprecision of the data. Polarization data are reduced and statistical uncertainties are stated using the standard deviation (SD) of the mean which represents a 68% confidence level (68% CL). For all cross-section data and results the uncertainty at the 98% confidence level (98% CL) has been adopted for the final statement of random error. For a sample of eight measurements the 98% CL is three standard deviations of the mean (3 SD), commonly used by other workers. Where warranted by a significant deviation in sample size from eight or nine measurements, Student's t distribution has been used to obtain the proper 98% CL (e.g., 3.75 SD for a sample of 5).

Where the uncertainty associated with a systematic effect could be evaluated in a separate experiment it has been stated at the 98% CL. The total uncertainty at the 98% CL represents a combination of stated imprecisions and systematic uncertainties. In a most conservative approach the individual uncertainties could be linearly added; but in a more realistic approach, if the separate uncertainties are judged to be uncorrelated, they should be combined in quadrature.

TABLE IV. Significant sources of uncertainty in evaluating the absolute photon detection sensitivity for the K filter. Uncertainties are expressed at the 98% confidence level.

Source of uncertainty	Percentage uncertainty Direct sum	Quadrature
Projected source area, $A\langle\sin\theta\rangle_\Omega$	0.8	0.6
Calculated strip lamp radiances, L_S		
Copper point (0.4 °K SD)	2.4	
Emissivity of W and transmission of quartz	2.0	3.1
Setting of and response to strip lamp, C_S		
Blackbody radiance fluctuations	0.6	
Random variation	2.0	2.3
Scintillator use	1.0	
Transfer factor C_F/C_C		
Random variation	2.2	
Systematic, see Sec. III E	5.4	3.6
Radiometric integrals $I_C/I_S/I_F$	2.2	2.2
Total uncertainty in $D(z_0, \lambda_K)$	18.6	5.6

Tables III and IV show uncertainty values for all the known significant sources in the experiment. Values of uncertainty from individual sources are combined in two ways. First, they are combined linearly. Second, uncorrelated uncertainties are combined in quadrature and then combined in quadrature with the linear sum of those which are possibly correlated. Table III shows for two electron energies all uncertainties except those associated with evaluating the absolute photon detection sensitivity, while the latter are shown in Table IV and are relevant for all energies. Combining the uncertainties in the two tables results in a total uncertainty in the absolute cross sections (at 4 eV) of about 37% by direct sum, and 10% (98% CL) by quadrature.

To the uncertainties resulting from the combination of entries in Tables III and IV must be added the one-sided uncertainties shown in Table II owing to scattered and secondary electrons. As the discussion in Sec. III B indicates, these one-sided uncertainties are probably considerably overestimated. Table III does not include the uncertainty ranging between 1% and 2% associated with allowance for the effect of space-charge depression by the electron beam, which enters when the cross section is determined from a plot, such as in Fig. 6.

V. POLARIZATION RESULTS

Results for the polarization of the K line are shown in Fig. 7. The uncertainties including systematic effects are given as standard deviations

by the error bars. At all energies the major source of uncertainty was statistical. Other sources of error or uncertainty beyond those discussed earlier are judged negligible. These include polarization of the detection system (0.1%) and possible misalignment of the polaroid by up to 3° with the relative velocity axis ($\Delta P/P \simeq 0.5\%$).

Percival and Seaton[19] give expressions for polarization of a ^2P to ^2S transition directly excited by electron impact. For the case of zero nuclear spin as is true for our Ca II target, the predicted polarizations are

$$P(^2P_{1/2} \rightarrow {}^2S) = 0, \quad P(^2P_{3/2} \rightarrow {}^2S) = 3(\sigma_0 - \sigma_1)/(5\sigma_0 + 7\sigma_1), \tag{17}$$

where σ_0 and σ_1 are partial cross sections for exciting the respective magnetic substates $M_L = 0$ and $M_L = 1$.

Saraph[20] has calculated the cross sections σ_M for exciting the ^2P multiplet (H and K together) using the reactance matrices from the three-state close-coupling calculation of Burke and Moores.[16] These were used to calculate the polarization of the multiplet. Her values can be used to get theoretical K-line polarizations P_K through the expression

$$P_K = 3P/(2 + \tfrac{1}{3}P). \tag{18}$$

The five theoretical polarizations so obtained are shown by the open circles in Fig. 7, where it is seen that the theoretical values are about 80% of those measured.

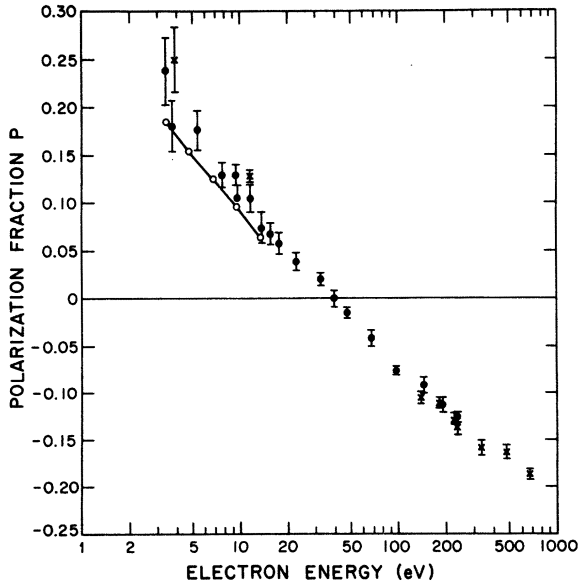

FIG. 7. Polarization fraction P [Eq. (7)] vs electron energy in eV. Crosses and dots were obtained about 1 yr apart. Flags represent standard deviations. Open circles connected by the line are calculated points of Saraph (Ref. 20).

For atomic systems Percival and Seaton[19] noted that at threshold $\sigma_1/\sigma_0 \rightarrow 0$. This allows a prediction of threshold polarization for such systems, and for an atomic system one would predict from Eq. (17) a threshold polarization of 0.60. We note, however, that such a prediction cannot be made for ion excitation; since, due to the Coulomb interaction, $\sigma_1/\sigma_0 \not\rightarrow 0$ necessarily at threshold. The threshold value for P as measured here is near 0.24. As pointed out[19] at high energies $\sigma_1/\sigma_0 \rightarrow \infty$, and the high-energy limit for polarization predicted from Eq. (17) in this case is −0.429. This prediction should be valid for ion excitation, and the data are consistent with this, though at the highest energy at which measurements were made the polarization is only 44% of the limiting value.

Measured polarizations of the H line are at 3.5 eV [−0.017 ±0.041], at 7.7 eV [−0.014 ±0.031], at 96.8 eV [−0.0046 ±0.0075], at 227 eV [−0.0047 ±0.0057], and at 237 eV [−0.002 ±0.010]. It is seen that in accord with the predictions of Eq. (17) the polarization is zero within the precision of the measurements.

VI. CROSS SECTIONS

Absolute cross sections for K-line emission are shown in Table V for those points obtained from plots of cross section versus electron current such as shown in Fig. 6. Energies are corrected values in eV, and column 2 of the table shows uncertainty in the energy. Column 3 shows the absolute cross section in units of 10^{-16} cm^2, column 4 shows uncertainty (98% CL) in percent including all effects except the absolute optical calibration, and column 5 shows the total absolute uncertainty (98% CL) in percent combining in

TABLE V. Absolute cross sections for exciting the K line as obtained from σ vs I plots. The uncertainty is given both with and without including the uncertainty in the absolute optical calibration, and is expressed at the 98% confidence level.

E eV	ΔE eV	$\sigma(E)$ 10^{-16} cm^2	$\Delta\sigma$% relative	$\Delta\sigma$% absolute
13.3	0.3	13.3	4.5	7.2
24.0	0.3	10.5	4.1	6.9
47.8	0.4	7.6	4.0	6.9
98.0	0.4	5.0	5.3	7.7
118.0	0.5	4.4	5.3	7.7
148.3	0.5	3.8	5.4	7.8
198.1	0.5	3.11	5.6	7.9
248.4	0.5	2.68	5.5	7.8
347.8	0.6	2.12	5.5	7.9
699.8	0.6	1.32	6.2	8.4

TABLE VI. Absolute cross sections with total uncertainties at the 98% confidence level for exciting the H emission and the ratio of cross sections for exciting the K and H emission.

E	σ_H 10^{-16} cm^2	$\Delta\sigma_H$ %	σ_K/σ_H	Uncertainty %
3.3	5.4	9.8	2.07	14
5.3	8.2	9.6	2.00	13
10.2	7.3	7.8	2.03	11
19.0	5.8	7.3	2.00	11
38.2	4.3	7.5	1.99	11
89.4	2.6	7.5	2.03	11
231.5	1.46	8.2	1.98	11
325	1.14	8.3	1.84	12
335	1.15	8.4	1.84	12

quadrature the 5.6% for optical calibration with numbers in column 4. The one-sided uncertainties of Table II have not been included in the listing.

Table VI gives H-line emission cross sections for several energies along with the total absolute uncertainty (98% CL) in percent. Column 4 shows the ratio of the K-line cross section to the H-line cross section, and column 5 the percentage uncertainty in this ratio. Data for this ratio were taken by alternately observing the K and H emissions, so form factor, drift, etc. played a minimum role in the determination.

In LS coupling the ratio of the cross sections for exciting the $^2P_{3/2}$ and the $^2P_{1/2}$ levels is in the ratio of the statistical weights, i.e., 2:1. The observed ratios are all 2:1 within the uncertainty of the measurements, and the average value for all energies of σ_K/σ_H is 1.98 ± 0.03 (SD).

Figure 8 shows a plot of the absolute cross section for K-line emission as a function of electron energy, giving a comparison between the measured values and some theoretical excitation cross sections. The low-energy theoretical values (B) represent the three-state close-coupling calculation of Burke and Moores,[16] and the classical binary-encounter calculation of Tripathi *et al.*[17] is also shown at low energies. Values at higher energy (S) are the Coulomb distorted-wave calculations of Burgess and Sheorey[18] using Hartree-Fock wave functions adjusted to give the experimental transition probability of Gallagher.[33] To make the comparison in the figure, the calculated multiplet excitation cross sections have been multiplied by $\frac{2}{3} \times 0.946 \times \pi a_0^2$ to get the K-line emission cross sections (0.946 is the branching ratio[33] between $4P \rightarrow 4S$ and $4P \rightarrow 3D$ transitions) in units of 10^{-16} cm^2.

In fact, of course, cascade from higher levels (Fig. 1) may also contribute to the population of the $4P$ level, and the measured emission cross section can be expressed

$$\sigma_{em}(4P \rightarrow 4S) = \gamma(4P \rightarrow 4S) \times \left(\sigma_{ex}(4S \rightarrow 4P) + \sum \gamma(nl \rightarrow 4P)\sigma_{ex}(4S \rightarrow nl)\right), \tag{19}$$

where σ_{em} denotes an emission cross section, σ_{ex} an excitation cross section, γ's are branching ratios, and the sum is over states n higher than $4P$. We must ask about the relative contribution of the terms in the summation sign to understand the validity of the comparison in Fig. 8. No direct measurements of these cascade terms were made, and we depend on three less direct sources to indicate the magnitudes of these terms: (i) measured[34,35] cascade contributions in K which is isoelectronic with Ca II, (ii) classical calculations of cascade terms by Burgess,[36] and (iii) structure in the measured cross section.

From their experimental investigation of the electron-impact excitation of K in the energy range from threshold to 30 eV, Zapesochnyi and

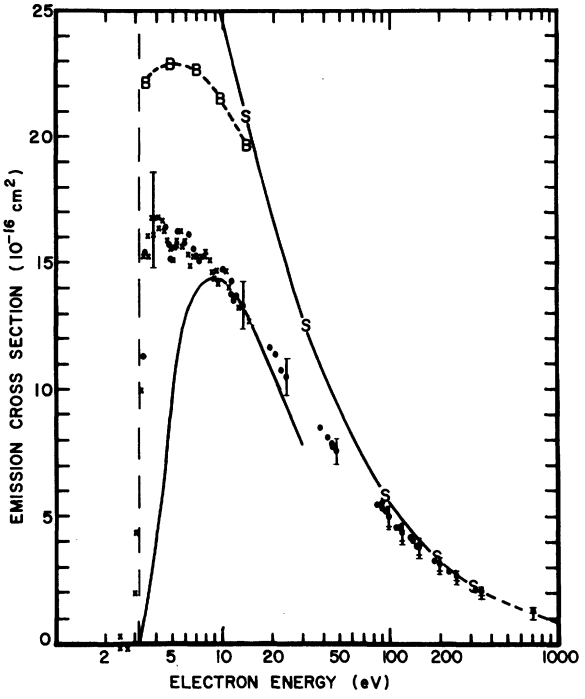

FIG. 8. Absolute emission cross sections for the K line (3934 Å) of Ca II as a function of incident electron energy. Crosses indicate data taken using interpolated form factors. Dots had individual form-factor measurements. Flags represent total error (random and systematic) at the 98% CL. Points B represent close-coupling calculations of Burke and Moores (Ref. 16). Points S are Coulomb distorted-wave calculations of Sheory and Burgess (Ref. 18). The solid curve going to 0 at threshold (vertical dashed line) is the classical binary-encounter calculation of Tripathi *et al.* (Ref. 17).

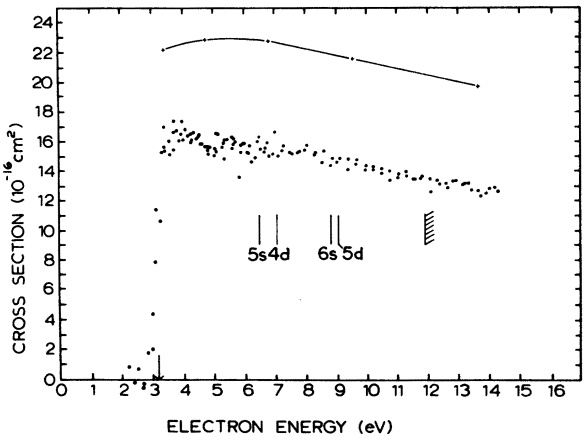

FIG. 9. Absolute emission cross section for the K line near threshold. Points were taken in scans and form factors obtained by interpolation (see text). The curve is the close-coupling calculation of Burke and Moores (Ref. 16).

Shimon[34] conclude that cascade from higher levels contributes about 10% to the observed resonance line emission. It can be inferred from their work[35] that approximately 63% of the cascade is from S states, approximately 37% is from D states, with 30% from the $3D$ state in particular (and that less than 1% arises from excitation of higher P states). In general the cross sections for exciting higher states decrease fairly rapidly with increasing principal quantum number. However, it should be mentioned that in K, cascade from the $4D$ state is anomalously low contributing only a fraction of 1% to the total cascade. Some care is needed in applying these results to the isoelectronic ion Ca^+. In this case the $3D$ level lies below the $4P$ level (Fig. 1) leading one to suspect that the total cascade contribution might be less than for K.

Burgess[36] has classically calculated cross sections for exciting the higher n levels (all l) suggesting a cascade contribution of 5% at the $5s$ threshold (6.5 eV) and 10% at the ionization threshold (11.9 eV). However this calculation is likely[36] to overestimate (perhaps by 50%) cascade. In the Bethe approximation,[37] valid at high energies, the cross sections for exciting the S and D levels fall off with energy as $1/E$ while the cross sections for the dipole-allowed resonance transitions fall off as $(\ln E)/E$. Thus at 250 eV the cascade contribution is likely to be less than (possibly only 50% of) the contribution at the ionization threshold.

Direct evidence for the smallness of the cascade contribution comes from an examination of Fig. 9. This shows the K-line cross section at low energies in greater detail and with more points than Fig. 8. Since the cross sections for exciting the cascade transitions are finite at threshold, the absence of any significant structure in the resonance line emission cross section at the $5S$ and $4D$ thresholds suggests that the combined cascade contribution from these two levels is probably less than 5%.

On the basis of the evidence cited we conclude that a reasonable assessment of cascade contributions is $5 \pm 3\%$ at the $5S$, $4D$ thresholds, $8 \pm 6\%$ at the ionization threshold, and $6 \pm 6\%$ above 250 eV. These contributions have neither been added to the theoretical curves nor subtracted from the experimental points in Figs. 8 and 9, and this must be borne in mind when making a comparison.

Referring again to Figs. 8 and 9 it is seen that the close-coupling results are about 1.45 times the measured values! Calculation of cross sections at low energies has long been a major challenge to theory, and it seems to be currently acknowledged that the close-coupling approach is the most reliable available method. For hydrogen excitation the method has predicted cross sections agreeing with experiment[38-40] within 10–15% after the addition of 20 electron-electron correlation terms.[41-43] Yet, the same success has not been achieved with He^+, where predictions[44,45] are still a factor of 2 higher than measured[46,47] cross sections which have been normalized to the Born approximation at high energies and corrected for a large amount of cascade. In sodium the success of the method has again been impressive, producing excellent agreement between experiment[48] and theory[49,50] in the range threshold to 5 eV.

In moving to more-complex systems such as the present case of Ca II, the close-coupling approximation is susceptible to additional errors arising from the use of approximate bound eigenstates. Since the Hartree-Fock radial wave functions used by Burke and Moores in the Ca^+ $4s$-$3d$-$4p$ calculation gave eigenenergies differing by 10% or more from the experimental ones, they solved the close-coupling equations using experimental energies. This procedure is not a self-consistent one and may actually give poorer cross sections, since different portions of the radial wave functions contribute to the expectation values of the energy and the dipole transition probability. Burke[51] has pointed out that a 35% discrepancy in the cross section between the close-coupling theory and experiment, is consistent with discrepancies of similar magnitude in the Ca atom resonance widths calculated in the same approximation. He suggests that to improve the calculation it will probably be necessary to include configuration-interaction effects in the target and perhaps to include more coupled channels in the collision process.

A dip in the cross section near 5 eV can be seen in both Figs. 8 and 9, and is reproducible in repetitive scans of σ at low energies. (Figure 9 is a composite of several such scans.) This feature lying 1.5 eV below the $5s$ level is probably associated with autoionizing levels belonging to the $5snl$ and $4dnl$ series. Autoionizing levels associated with the $4pnl$ and $3dnl$ series have been observed optically,[52-54] but observations did not extend to short enough wavelengths to observe the level(s) involved here.

Taking into account the measured spread in electron energies [Eq. (9)], the expected[55] finite cross section at threshold is strikingly demonstrated by the results in Figs. 8 and 9. This feature has a profound effect[56,57] upon rates in plasmas where one averages over a thermal distribution of velocities. Emission coefficients α obtained by averaging measured cross sections times velocity are shown for the K line in Fig. 10 where $\alpha\, e^X$ is plotted versus temperature. Here $X = E_{\rm th}/kT = 36\,566\ ^\circ{\rm K}/T$, and units are 10^{-7} cm^3 sec^{-1}. If one assumes a constant cross section past threshold of 16×10^{-16} cm^2, the K-line emission coefficient is $\alpha = 1.90\times10^{-7}X^{-1/2}(X+1)e^{-X}$. Values computed from this expression agree to better than 1% with the numerically integrated values shown in Fig. 10 out to about 10^4 °K. At 2×10^4 °K the above form gives a value 1.5% too high, and at 10^5 °K it gives a value 30% too high.

The classical calculation of Tripathi *et al.*[17] does not exhibit the finite cross section at threshold, and at energies above 20 eV clearly shows a divergent shape. However, near the peak of the classical function in the range 7–30 eV the magnitude of this calculation is in (10%) agreement with the measured values. It is difficult to assess the significance of this agreement, but the fact is worthy of note. The emission coefficient computed using this cross section is also shown in Fig. 10.

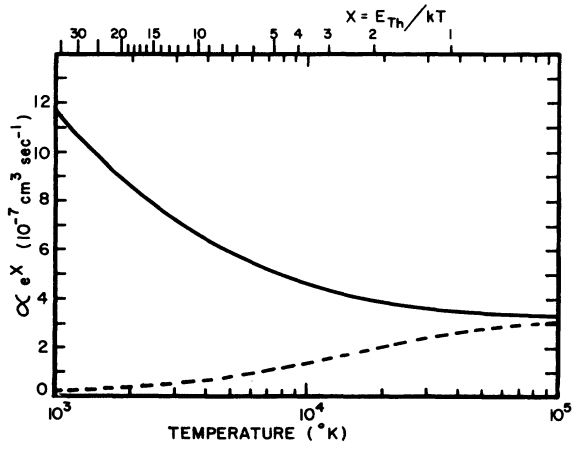

FIG. 10. K-line emission coefficient α times e^X (where $X = 36\,566\ ^\circ{\rm K}/T$) as a function of T computed using a Boltzmann distribution of electron velocities. Solid curve used measured cross sections and the dashed curve used the classical cross section of Tripathi *et al.* (Ref. 17).

Figure 8 shows the Coulomb distorted-wave calculations of Burgess and Sheorey[18] merging with the measured cross sections at high energies. This comparison is better viewed in another way, however. It is well known that the product of cross section and energy is generally a relatively slowly varying function of energy which at sufficiently high E, assumes the form

$$\sigma E = A\ln E + B, \tag{20}$$

where the constants are provided by the Bethe approximation. Thus a plot of σE vs $\ln E$ provides a more revealing comparison with theory at moderate and high energies and also is a useful test for energy dependent systematic errors in the experiment. To make this comparison we have converted the measured emission cross section for the K line into a cross section for excitation of the $4p$ multiplet by dividing by the factor $(\frac{2}{3}\times0.947\times\pi a_0^2)$. The product $\Omega = \sigma_{\rm ex}E$ is then the total collision strength for excitation of the $4p$ multiplet

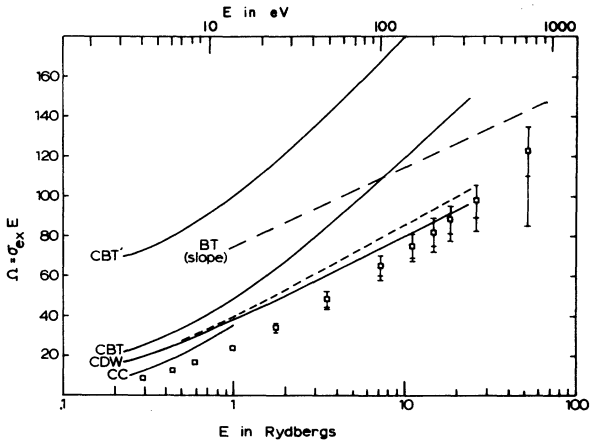

FIG. 11. Comparison of theoretical and experimental collision strengths for the Ca II $4s \rightarrow 4p$ transition. BT = Bethe asymptotic slope based on oscillator strength of Gallagher (Ref. 33). CBT′ = nonunitarized Coulomb-Bethe (Ref. 18). CBT = unitarized Coulomb-Bethe (Ref. 18). CDW = Coulomb distorted-wave calculations (Ref. 18) where the dashed curve was computed with Hartree-Fock wave functions adjusted to give bound-state eigenenergies in agreement with experiment, and the continuous curve is based on wave functions modified to more nearly give the experimental oscillator strength of Gallagher (Ref. 33). CC = $4s$-$3p$-$4d$ close coupling (Ref. 16). Experimental points include cascade estimated to be 6 ±6% at 250 eV. Flags are 98% confidence limits on the absolute collision strength.

except that the result needs to be reduced according to the amount of cascade.

In Fig. 11 it can be seen that above 25 Ry the experimental cross section is merging with the Coulomb-distorted-wave calculations of Burgess and Sheorey[18] (which at these energies are almost identical with their Coulomb-Born calculations—see Fig. 2). As expected, the calculation based on bound-state wave functions, which gives more nearly the measured[33] dipole transition probability, rather than the correct bound-state energies, is more in line with the experimental cross section. The Coulomb-Bethe approximation, which includes only the long-range part of the interactions occuring in the Coulomb-Born, appears to be diverging from both the Coulomb-Born and the plane-wave Bethe calculations. (Burgess and Sheorey used the nonunitarized Coulomb-Bethe approximation to calculate the contribution to the collision strength from large values of the angular momentum; these remain significant in Coulomb-Born calculations for positive ions.)

An examination of Fig. 11, recognizing the presence of a cascade contribution in the experimental cross section of about $6 \pm 6\%$ at about 20 Ry leads to the following comments: (a) The experimental collision strength has probably not yet reached the Bethe regime (where the slope of σE vs $\ln E$ decreases into agreement with the Bethe asymptotic slope) at an energy of 25 Ry (110 thresholds). (b) The highest-energy points may be too large, as allowed for in the error bars, due to the presence of low-energy secondary electrons in the beam. (c) At 25 Ry the absolute cross section is in agreement with the Coulomb-Born calculation well within the experimental uncertainty ($\pm 8\%$ plus uncertainty in cascade) and also within the uncertainty of the calculation, which Burgess[36] estimates at around $\pm 10\%$ in this energy range.

That the Born regime is not reached at lower energy may seem surprising in the light of other cases ($1s \rightarrow 2s$, $1s \rightarrow 2p$ transitions in H, $1s \rightarrow 2s$ in He^+) where it appears to be reached at less than 20 thresholds. However, these generally involve simple atoms with relatively high threshold energies. In studying the resonance transition in Na, for which the threshold is 2.1 eV, Enemark and Gallagher[48] found that in going from high to lower energies the experimental collision strength began to diverge from the Born results at 250 eV or 120 thresholds, the divergence being 1.3% at 250 eV and 6.2% at 100 eV.

ACKNOWLEDGMENTS

The authors gratefully acknowledge the close collaboration of Dr. D. H. Crandall, Dr. K. T. Dolder, and Dr. W. E. Kauppila on different phases of the experiment. They thank Dr. V. J. Sheorey, Dr. Alan Burgess, and Dr. P. G. Burke for helpful discussions and communications.

---

*Work supported in part by the Controlled Thermonuclear Division of the U. S. Atomic Energy Commission.

†Present address: School of Physics, University of Newcastle-upon-Tyne, Newcastle-upon-Tyne, England.

[1]B. L. Moiseiwitsch and S. J. Smith, Rev. Mod. Phys. 40, 238 (1968).

[2]M. F. A. Harrison, Brit. J. Appl. Phys. 17, 371 (1966).

[3]K. T. Dolder, in *Case Studies in Atomic Collision Physics*, edited by E. W. McDaniel and M. R. C. McDowell (North-Holland, Amsterdam, 1969).

[4]G. H. Dunn, in *Atomic Physics*, edited by V. W. Hughes, V. W. Cohen, and F. M. J. Pichanick (Plenum, New York, 1969), p. 417.

[5]D. F. Dance, M. F. A. Harrison, and A. C. H. Smith, Proc. Roy. Soc. Lond. A290, 74 (1966).

[6]G. H. Dunn and B. Van Zyl, Phys. Rev. 154, 40 (1967).

[7]D. F. Dance, M. F. A. Harrison, R. D. Rundel, and A. C. H. Smith, Proc. Phys. Soc. Lond. 92, 577 (1967).

[8]B. Peart and K. T. Dolder, J. Phys. B 4, 1496 (1971).

[9]A. R. Lee and N. P. Carlton, Phys. Lett. A 27, 195 (1968).

[10]F. M. Bacon and J. W. Hooper, Phys. Rev. 178, 182 (1969).

[11]M. O. Pace and J. W. Hooper, Phys. Rev. A 7, 2033 (1973).

[12]For example, see J. L. Linsky and E. H. Avrett, Publ. Astron. Soc. Pac. 82, 169 (1970).

[13]J. T. Jefferies, Aust. J. Phys. 7, 22 (1954).

[14]H. van Regemorter, Mon. Not. R. Astron. Soc. 121, 213 (1960).

[15]D. Petrini, C. R. Acad. Sci. (Paris) 260, 4929 (1965).

[16]P. G. Burke and D. L. Moores, J. Phys. B 1, 575 (1968).

[17]A. N. Tripathi, K. C. Mathur, and S. K. Joshi, Phys. Rev. A 1, 337 (1970).

[18]A. Burgess and V. B. Sheorey (unpublished).

[19]I. C. Percival and M. J. Seaton, Philos. Trans. R. Soc. Lond. A 251, 113 (1958).

[20]H. E. Saraph, J. Phys. B 3, 952 (1970).

[21]P. O. Taylor, Ph.D. thesis (University of Colorado, Boulder, Colo., 1972) (unpublished). Available through University Microfilms, Inc., Ann Arbor, Mich.

[22]P. O. Taylor, K. T. Dolder, W. E. Kauppila, and G. H. Dunn (unpublished).

[23]L. Harris and J. K. Beasley, J. Opt. Soc. Am. 42, 134 (1952).

[24]A. V. Haeff, Proc. IRE 27, 586 (1939).

[25]H. S. W. Massey and E. H. S. Burhop, *Electronic and Ionic Impact Phenomena* (Oxford U. P., London, 1969), Vol. 1, p. 101.

[26]R. K. Asundi, Proc. Phys. Soc. Lond. 82, 372 (1963).
[27]D. Rapp and P. Englander-Golden, J. Chem. Phys. 43, 1464 (1967).
[28]B. L. Schram, H. R. Moustafa, J. Schutten, and F. J. de Heer, Physica (Utr.) 32, 734 (1966).
[29]N. R. Whetten, in *Methods in Experimental Physics*, edited by V. W. Hughes and H. L. Schultz (Academic, New York, 1962), Vol. 4A, p. 69.
[30]W. A. Shurcliff and S. S. Ballard, *Polarized Light* (Van Nostrand, New York, 1964), p. 69.
[31]R. D. Lee, *Construction and Operation of a Simple High-Precision Copper Point Black Body and Furnace*, Nat. Bur. Std. Tech. Note No. 483 (U.S. GPO Washington, D.C., 1969).
[32]The statistical uncertainty or standard deviation on a counting measurement is the square root of the accumulated counts. The standard deviation *about* the mean, $\bar{x}$, of a sample of n measurements, x_i, is $S=\{[\sum(x_i-\bar{x})^2]/n-1\}^{1/2}$. The standard deviation (SD) of the mean of a sample of n measurements is $S/\sqrt{n}$, and represents a 68% confident interval.
[33]A. C. Gallagher, Phys. Rev. 157, 24 (1967).
[34]I. P. Zapesochnyi and L. L. Shimon, Opt. Spektrosk. 21, 261, (1966) [Opt. Spectrosc. 21, 155 (1966)].
[35]I. P. Zapesochnyi, I. P. Shimon, and A. K. Soshnikov, Opt. Spektrosk. 19, 864 (1965) [Opt. Spectrosc. 19, 480 (1965)].
[36]A. Burgess (private communication).
[37]S. Geltman, *Topics in Atomic Collision Theory* (Academic, New York, 1969), Chap. 14.
[38]R. L. Long, D. M. Cox, and S. J. Smith, J. Res. Natl. Bur. Std. (U.S.) A 72, 521 (1968).
[39]J. W. McGowan, J. F. Williams, and E. K. Curley, Phys. Rev. 180, 132 (1969).
[40]W. E. Kauppila, W. R. Ott, and W. L. Fite, Phys. Rev. A 1, 1099 (1970).
[41]P. G. Burke, S. Ormonde, and W. Whitaker, Proc. Phys. Soc. Lond. 92, 319 (1967).
[42]A. J. Taylor and P. G. Burke, Proc. Phys. Soc. Lond. 92, 336 (1967).
[43]P. G. Burke, A. J. Taylor, and S. Ormonde, Proc. Phys. Soc. Lond. 92, 345 (1967).
[44]P. G. Burke, D. D. McVicar, and K. Smith, Proc. Phys. Soc. Lond. 83, 397 (1964).
[45]P. G. Burke and A. J. Taylor, J. Phys. B 2, 44 (1969).
[46]D. F. Dance, M. F. A. Harrison, and A. C. H. Smith, Proc. Roy. Soc. A 290, 74 (1966).
[47]B. Peart and K. T. Dolder (private communication).
[48]E. A. Enemark and A. Gallagher, Phys. Rev. A 6, 192 (1972).
[49]D. L. Moores and D. W. Norcross, J. Phys. B 5, 1482 (1972).
[50]D. F. Korff, S. Chung, and C. C. Lin, Phys. Rev. A 7, 545 (1973).
[51]P. G. Burke (private communication).
[52]R. W. Ditchburn and R. D. Hudson, Proc. Roy. Soc. A 164, 167 (1960).
[53]W. R. S. Garton and K. Codling, Proc. Phys. Soc. Lond. 86, 1067 (1965).
[54]G. H. Newsom, Proc. Phys. Soc. Lond. 87, 975 (1966).
[55]M. J. Seaton, in *Atomic and Molecular Processes*, edited by D. R. Bates (Academic, New York, 1962), p. 374.
[56]J. L. Schwob, J. Phys. (Paris) 25, 713 (1964).
[57]H. W. Drawin, Ann. Phys. (Leipz.) 16, 195 (1965).